

# Imaging of Crystal Morphology and Molecular Simulations of Surface Energies in Pentacene Thin Films

Lawrence F. Drummy,<sup>†</sup> Paul K. Miska,<sup>‡</sup> David Alberts, Nuram Lee, and David C. Martin\*

Department of Materials Science and Engineering and Macromolecular Science and Engineering Center, 2022 H. H. Dow Building, University of Michigan, Ann Arbor, Michigan 48109-2136

Received: September 1, 2005; In Final Form: December 20, 2005

We have investigated the crystal growth of the organic semiconductor pentacene by complementing molecular simulations of surface energies with experimental images of pentacene films. Pentacene thin films having variations in thickness and grain size were produced by vacuum sublimation. Large ( $\sim 20\ \mu\text{m}$ ) faceted crystals grew on top of the underlying polycrystalline thin film. The films were characterized using optical microscopy (OM), X-ray diffraction (XRD), scanning electron microscopy (SEM), and transmission electron microscopy (TEM). Single crystals most commonly grew in a truncated diamond shape with the largest crystal face, (001), growing parallel to the substrate. Crystal morphologies and surface energies were calculated using force field-based molecular simulations. The (001) surface was found to have the lowest energy, at  $76\ \text{mJ}/\text{m}^2$ , which was consistent with experimental observations of crystal face size. It was demonstrated that the morphology of the large faceted crystals approached the equilibrium growth shape of pentacene. From contact angle measurements, the critical surface tension of textured pentacene thin films in air was determined to be  $34\ \text{mJ}/\text{m}^2$ .

## Introduction

Pentacene and other conjugated molecules are of current interest for use as the active layer in organic field effect transistors. Pentacene is a highly crystalline material with a relatively large degree of  $\pi$ -orbital overlap, and this overlap promotes high charge carrier mobility. Room-temperature carrier mobilities on the order of  $1\ \text{cm}^2\ \text{V}^{-1}\ \text{s}^{-1}$  have been measured from thermally evaporated thin films.<sup>1–4</sup> Pentacene has a triclinic structure ( $P\bar{1}$ ) with two molecules in the unit cell and the following lattice parameters:  $a = 0.628\ \text{nm}$ ,  $b = 0.771\ \text{nm}$ ,  $c = 1.444\ \text{nm}$ ,  $\alpha = 76.75^\circ$ ,  $\beta = 88.01^\circ$ ,  $\gamma = 84.52^\circ$ , and  $\rho = 1.365\ \text{g}/\text{cm}^3$ .<sup>5</sup> This crystal structure has been experimentally determined by X-ray diffraction from large ( $\sim 1\ \text{cm}$ ) single crystals grown via both solution growth under vacuum<sup>5</sup> and growth from the vapor in an inert gas atmosphere.<sup>6</sup> Like many aromatic molecules, pentacene packs in a herringbone arrangement in the  $a$ – $b$  plane. The  $c$ -axis is significantly longer than the  $a$ - or  $b$ -axis and is assigned to the vector closest to the (001) normal. The (001) plane spacing, which is  $1.41\ \text{nm}$ , is much larger than any other and becomes a signature spacing for the crystal. Thin films of triclinic bulk phase pentacene, described well by the structure described above, can be produced by thermal evaporation of films greater than  $100\ \text{nm}$  in thickness onto substrates held at elevated temperatures ( $50$ – $100\ ^\circ\text{C}$ ).<sup>2,7–9</sup>

Many researchers have also characterized a unique “thin-film” phase of pentacene. The thin-film phase appears in films with a thickness of generally less than  $100\ \text{nm}$  grown on substrates held at room temperature or colder, and it has an interlayer spacing ranging from  $1.50$  to  $1.55\ \text{nm}$ .<sup>2,7–11</sup> The two processing

parameters that most reproducibly cause a phase transformation in pentacene are film thickness and substrate temperature.<sup>7,8</sup> Variation of these two parameters can produce films with both the bulk phase and thin-film phase present. The thin-film phase has been found to grow in intimate contact with the substrate, and then at an apparently critical thickness, the bulk phase begins to form.<sup>8</sup> An orthorhombic crystal structure has been determined for the thin-film phase of pentacene.<sup>12</sup> The crystals had four molecules in the unit cell and the following lattice parameters:  $a = 0.59 \pm 0.02\ \text{nm}$ ,  $b = 0.74 \pm 0.02\ \text{nm}$ , and  $c = 3.00 \pm 0.08\ \text{nm}$ . In this structure, the molecules retain their herringbone packing in the  $a$ – $b$  plane, and they also form a herringbone along the  $c$ -axis.

The molecular reorganization near symmetry-breaking defects such as dislocations, grain boundaries, and free surfaces is likely to influence both the mechanical and electrical properties of pentacene thin films.<sup>10,12,13</sup> We have studied the growth, morphology, and free surfaces of thermally evaporated pentacene films. Images of crystal morphologies were compared to equilibrium growth shapes predicted from simulations of crystal surface energies. Many thin films of pentacene shown in the literature exhibit a “fern”-like or dendritic morphology, which is attributed to a diffusion-limited growth process.<sup>2,14,15</sup> Some films have shown faceting, however, and the (001) and (110) type planes were clearly visible in AFM and SEM images.<sup>8,16</sup> Optimizing charge carrier mobility by tailoring crystal grain size and morphology in electronically active organic thin films has been achieved in thin films of copper phthalocyanine.<sup>17</sup> Larger grain sizes were found to improve the transport properties of these films, due to a decrease in the number of transport-limiting grain boundaries. However, when the grains were too large, holes between grains became the major transport-limiting defects.

The surface energies of pentacene have recently been calculated using first-principles pseudopotential density-func-

\* To whom correspondence should be addressed. E-mail: milty@umich.edu.

<sup>†</sup> Present address: Air Force Research Laboratories, 2941 Hobson Way, Building 654, Wright Patterson Air Force Base, OH 45424.

<sup>‡</sup> Present address: ArvinMeritor, 2135 W. Maple Rd., Troy, MI 48084.

tional theory.<sup>18</sup> It was found that the (001) surface had a much lower energy than any other. Kitaigorodsky calculated the surface energies of anthracene, the three-ring aromatic analogue of pentacene, using an attachment energy calculation.<sup>19</sup> While the equilibrium growth shapes of organic crystals<sup>20</sup> have long been of interest to the pharmaceuticals industry, recent developments in the field of plastic electronics have demonstrated the need to study the thermodynamics of crystallization of electrically active organic molecules. Empirical force fields have been used to successfully predict the structure and properties of collections of atoms. The Dreiding force field<sup>21</sup> was developed to predict the structure and dynamics of organic, biological, and inorganic molecules. The force field uses general force constants based on simple hybridization considerations rather than individual force constants that depend on the particular combination of atoms involved in the calculation. Nonbonded van der Waals interactions are described by an exponential-6 Buckingham potential expression of the form

$$E_{\text{vdW}} = Ae^{-Cr} - Br^{-6}$$

Dreiding has been proven to competently predict the structures<sup>22</sup> and mechanical properties<sup>22</sup> of many molecular and polymer crystals.

Here we will investigate the crystal structure and morphology in thermally evaporated pentacene films. X-ray and electron diffraction are used to determine the crystal structure, the degree of film texturing, and the internal perfection of individual crystal grains within the films. Using SEM, a faceted single-crystal morphology was characterized, from which the area of each crystallographic face was determined. The relative crystal face areas were compared with atomistic surface energy calculations. Finally, contact angle measurements on textured thin films were used to determine the pentacene surface tension in air. A complete description of the crystal structure, defects, and morphology in pentacene thin films will be critical for the application of this material in real devices.

## Experimental Section

Pentacene powder as received from Aldrich was sublimed in a glass tube approximately 2 cm in diameter held under a vacuum of  $\sim 10^{-4}$  Torr. A flame heat source was held at the end of the tube containing the source powder, and this created a temperature gradient along the tube. The substrates used were amorphous carbon-coated mica and uncoated mica placed approximately 1–2 cm from the source pentacene powder.

Thermally evaporated thin films were removed from the substrates and formed into a powder for initial XRD analysis. A Rigaku rotating anode X-ray diffractometer with Cu K $\alpha$  radiation was used to generate the powder X-ray pattern. A Bede diffractometer with Cu K $\alpha$  radiation was used for X-ray diffraction on textured thin films. Optical microscopy was carried out using a Nikon Optiphot with crossed polarizers. SEM was carried out on a Philips XL30 FEG device operating at 5 kV, and TEM was carried out on a JEOL 4000 EX device operating under low-dose conditions<sup>23</sup> at 400 kV. The total end point dose for destruction of crystallinity of pentacene at 400 kV is  $0.25 \pm 0.05$  C/cm<sup>2</sup>.<sup>13</sup> All electron diffraction patterns were taken at a dose of  $10^{-4}$ – $10^{-3}$  C/cm<sup>2</sup>. Droplets produced for contact angle measurements were several millimeters in size, much larger than the grain size of the films, and they were imaged using an optical microscope with the viewing direction parallel to the horizontal film surface.

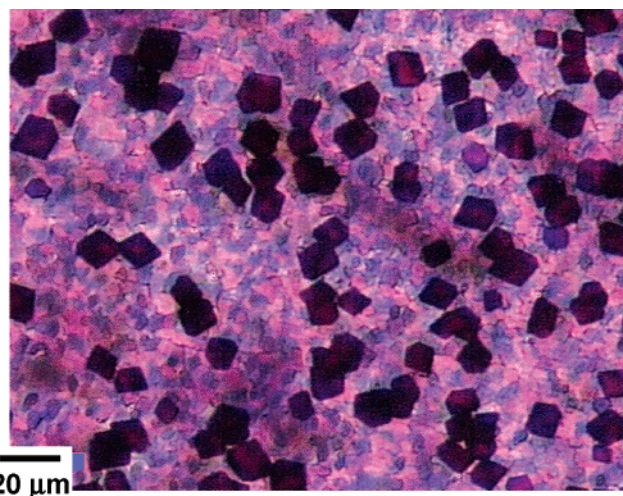


**Figure 1.** Optical micrograph of a sublimed pentacene film grown on mica.

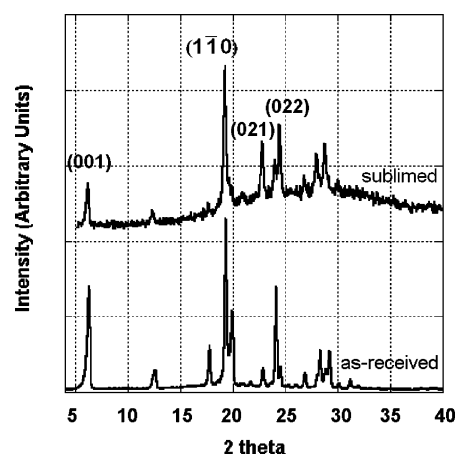


**Figure 2.** Powder XRD of pentacene crystals before and after sublimation.

The molecular modeling software package Cerius<sup>2</sup> version 4.6 was used for simulation of pentacene surface energies. Pentacene lattice parameters and atomic coordinates were entered into the model directly from experimentally determined structural data.<sup>5</sup> The Dreiding 2.21 force field was used to balance the charges in the unit cell, to calculate the energy of the crystal, and to minimize the lattice energy by varying the lattice parameters and atom positions using the “Smart Minimizer” which incorporates the steepest descent, conjugate gradient, and Newton–Raphson methods.

## Results and Discussion

Pentacene powder was thermally evaporated onto amorphous carbon-coated mica substrates to form crystallographically textured thin films. Figure 1 shows an optical micrograph of a sublimed pentacene thin film taken under crossed polars. In the micrograph, two different morphologies can be seen. A well-connected polycrystalline thin film of pentacene was grown directly on the amorphous carbon substrate. On top of this film grew a second layer of larger, faceted single crystals that had a truncated diamond morphology and were 10–20  $\mu\text{m}$  in size. Powder XRD (Figure 2) done before and after sublimation showed slight changes in peak positions and intensities.  $\theta/2\theta$  diffraction from thermally evaporated thin films typically yields only (001) peaks, because of the high degree of (001) film texturing. This gives only a limited amount of crystal structure

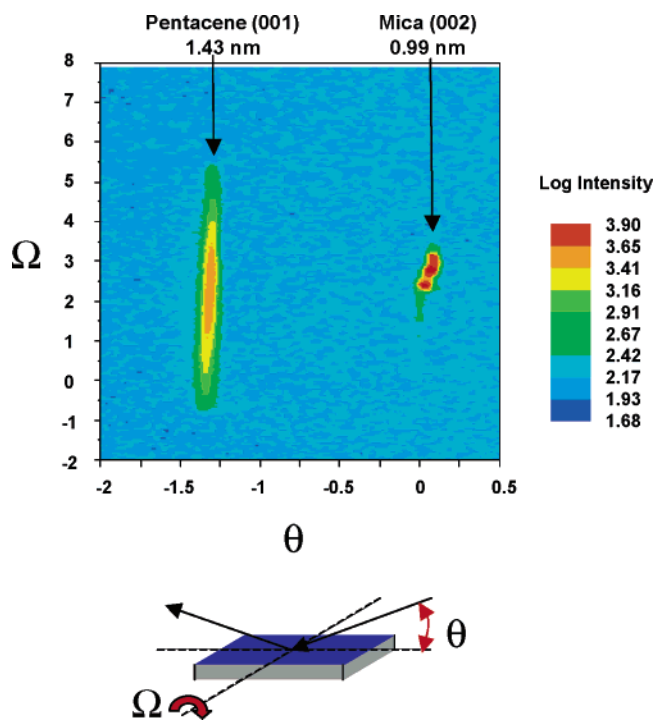


**Figure 3.** Reflection XRD in the  $\theta/2\theta$  geometry of a textured thin film of pentacene. The x-axis is  $\theta$  in units of degrees centered at the mica (002) peak. The y-axis is  $\Omega$ , the degree of substrate tilt about an axis in the plane of the film and perpendicular to the incident beam direction.

information, and because of this, the films were removed from the substrate and formed into a powder. Any deformation caused by this process is unlikely to cause changes to the crystal structure.<sup>13</sup> The spacing of the (001) planes before sublimation was 1.40 nm, and this was in good agreement with the experimental unit cell determined by Holmes and co-workers.<sup>5</sup> One of the most intense reflections in the powder pattern was the (022) peak measured at 0.37 nm. After sublimation, the (001) peak shifted slightly to 1.43 nm, and the (021) reflection at 0.39 nm increased in intensity relative to the (022) reflection at 0.37 nm, indicating the molecules were slightly tilted up toward the substrate normal. In the bulk crystal structure determined by Holmes et al., the long axes of the molecules lie in the (022) planes, giving these planes strong diffraction intensity. After sublimation, the molecules tilted up toward the substrate, thus increasing the intensity of the (021) peak relative to the (022) peak and slightly increasing the (001) plane spacing. The differences in crystal structure between triclinic single crystals and triclinic thin films of pentacene have also been discussed elsewhere.<sup>6,24</sup>

We used XRD, TEM, and ED to investigate the crystallography and defects in the thermally evaporated pentacene films. It has been shown previously that polycrystalline pentacene thin films commonly grow with the long axis of the molecules nearly perpendicular to the substrate.<sup>10</sup> To investigate the degree of crystallographic texturing of the films, we carried out XRD in the  $\theta/2\theta$  geometry, while varying the degree of substrate tilt. Figure 3 shows a contour map of the diffraction intensity in counts as a function of  $\theta$  (x-axis) and substrate tilt  $\Omega$  (y-axis). The 0.99 nm mica (002) peak is visible, along with the 1.43 nm pentacene (001) peak. The diffraction intensity of the (001) pentacene peak dropped significantly at a tilt of  $3^\circ$ , indicating that the (001) planes were nearly parallel to the substrate across the entire film.

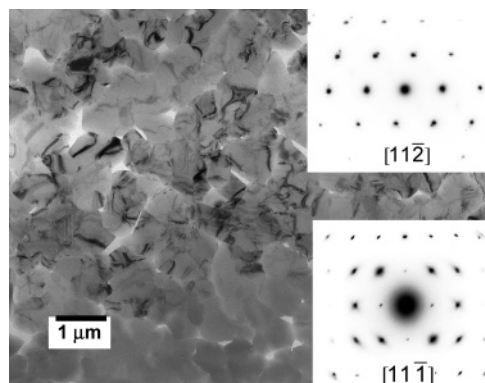


**Figure 4.** Bright field TEM micrograph of a textured pentacene thin film with selected area electron diffraction patterns from different single crystalline regions of the film.

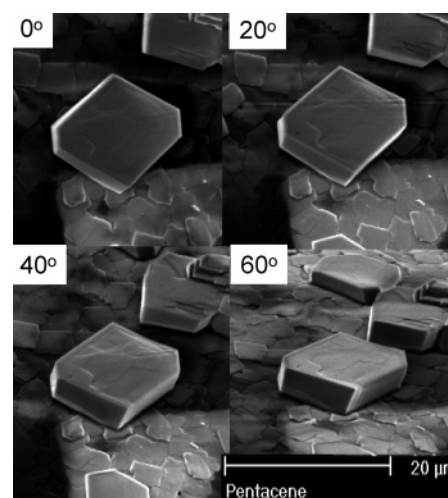


**Figure 5.** SEM tilt series on a pentacene single crystal.

Figure 4 shows a bright field TEM micrograph of a pentacene film oriented in plan view with a selected area electron diffraction (SAED) pattern from two different single-crystal grains. The  $[11\bar{1}]$  orientation corresponds to the direction looking down the long axis of the molecules. Because of the high degree of (001) texturing parallel to the substrate, a more common projection for films oriented in plan view is the  $[11\bar{2}]$ , which is close to the (001) normal. The dark stripes inside the crystal grains in the TEM image are diffraction contrast from bend contours. Under electron beam irradiation, the bend contours move, interacting with each other and defects in the crystal, and they eventually disappear when the crystals are fully amorphous. A region of irradiated amorphous pentacene crystals free of bend contours can be seen running horizontally across the bottom of the figure.

We used scanning electron microscopy to measure the areas of the pentacene single-crystal faces in the films. The morphology of single crystals was regular, with faceting observed primarily on the (001), (110),  $(-110)$ , and (010) faces only. Figure 5 shows a tilt series of a pentacene single crystal, exhibiting the common truncated diamond shape, from 0 to  $60^\circ$  in increments of  $20^\circ$ . With careful control of the tilt axis and tilt angle, it was possible to measure the crystal face areas for a large number of single crystals. The measured crystal face areas of the (110) type and (010) surfaces are plotted in Figure 6 versus the measured (001) surface area. A linear fit through the zero of the data gives an  $A_{110}$  of  $0.37A_{001}$  and an  $A_{010}$  of  $0.08A_{001}$ . These numbers were used for comparison with predictions from molecular simulations.



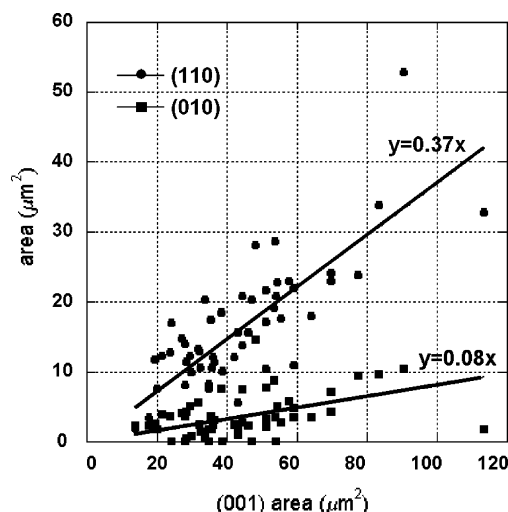


**Figure 6.** Plot of the experimentally measured (110) and (010) crystal face areas plotted vs the (001) plane area measured from many crystals in the SEM images. The lines represent a linear fit through zero.

**TABLE 1: Comparison of Experimentally Measured Pentacene Lattice Parameters from ref 5 and Lattice Parameters Determined from the Dreiding Simulated Minimum Energy Crystal Structure**

	<i>a</i> (nm)	<i>b</i> (nm)	<i>c</i> (nm)	$\alpha$ (deg)	$\beta$ (deg)	$\gamma$ (deg)	$\rho$ (g/cm <sup>3</sup> )
experimental	0.628	0.771	1.444	76.75	88.01	84.52	1.365
Dreiding	0.645	0.802	1.432	77.80	89.31	86.07	1.280
difference	+2.6%	+3.9%	−0.8%	+1.3%	+1.5%	+1.8%	−6.6%

**TABLE 2: Simulated Surface Energies,  $\sigma$ , and Attachment Energies,  $E_{\text{att}}$ , of Pentacene Low-Index Faces, along with the Predicted and Measured Crystal Face Areas**

crystal surface	(001)	(010)	( $\bar{1}10$ )	(110)
$\sigma$ (mJ/m <sup>2</sup> )	76	140	130	150
$E_{\text{att}}$ (mJ/m <sup>2</sup> )	−74	−142	−129	−151
$A_{(hkl)}/A_{(001)}$ (calculated)	1	0.08	0.35	0.32
$A_{(hkl)}/A_{(001)}$ (measured)	1	0.08	0.37	0.37

The Cerius<sup>2</sup> version 4.6 molecular modeling software package was used to simulate the surface energies of low-index crystallographic faces in pentacene. The procedure was to begin with the model according to the atomic coordinates by Holmes et al. and minimize the system energy with all unit cell constraints open. The lattice parameters of the structure before and after minimization using the Dreiding force field are shown in Table 1. Each lattice parameter was expanded separately by incremental amounts, calculating the total energy of the system at each step. Surface reconstruction was not taken into account in the simulations, as energy minimizations after the lattice parameter expansion were not performed. The plot of total energy versus the length of the *c*-axis is shown in Figure 7. A minimum can be seen at the equilibrium length, which is 1.43 nm. As the *c*-axis is compressed, the energy rises sharply, and as *c* expands, the energy rises and converges to a value whose difference from the energy of the perfect crystal is the energetic cost of creating a new surface. To simulate the energy of the (110) type surfaces, the lattice of the minimized crystal structure was redefined so that  $a \rightarrow [110]$ ,  $b \rightarrow [-110]$ , and  $c \rightarrow [001]$ . The *a*- and *b*-axes of this crystal were then expanded separately to calculate the (110) surface energy. The surface energies of the low-index planes are given in Table 2, converted to units of millijoules, and normalized by the area of the surface created.

To display the crystal morphology, we used the Hartman–Perdok method<sup>25</sup> to calculate the attachment energies of the growth faces of pentacene and the Wulff plot method<sup>26</sup> for

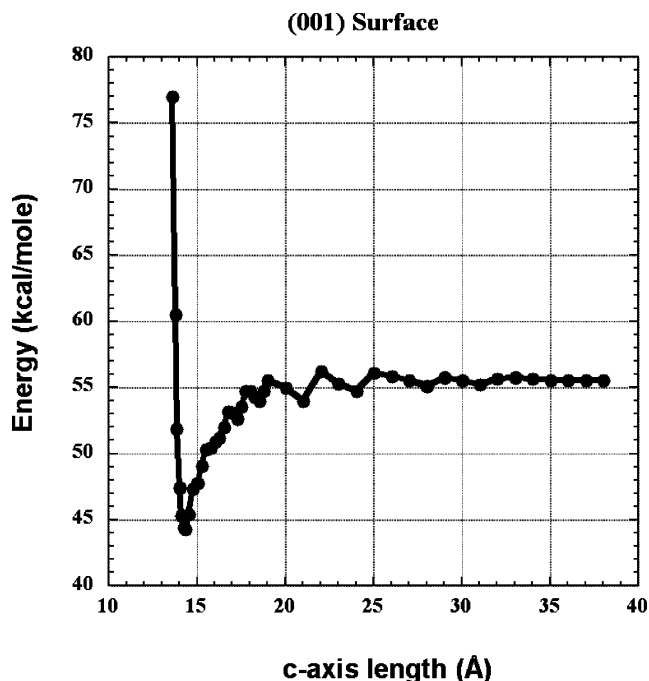


**Figure 7.** Plot of the simulated energy of the pentacene crystal as a function of the length of the *c*-axis. The difference between the energy at the equilibrium length ( $c = 1.43$  nm) and the energy as  $c \rightarrow \infty$ , normalized by the area of the (001) surface, is equal to the (001) surface energy.

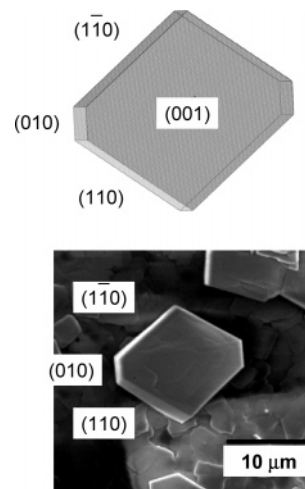


**Figure 8.** Simulated crystal morphology, with crystallographic faces labeled, compared to an experimental SEM image of a thermally evaporated pentacene single crystal.

visualization. The attachment energy is defined as the energy released upon the attachment of a growth slice to a crystal surface. The calculated attachment energies are listed in Table 2, and the absolute value of the attachment energy shows good agreement with the calculated surface energy values. The resulting crystal morphology, with only crystal faces seen experimentally displayed, is shown in Figure 8. The Cerius<sup>2</sup> attachment energy module predicts more crystallographic facets should be present than are observed experimentally. These additional facets were deleted from the Wulff plot for comparison with the data. The simulated relative face areas are listed in Table 2, along with those measured from the experimental images of crystals. When only the crystal faces observed experimentally are considered, the agreement between the measured and predicted face areas is very good. This demonstrates that our growth process is close to thermodynamic

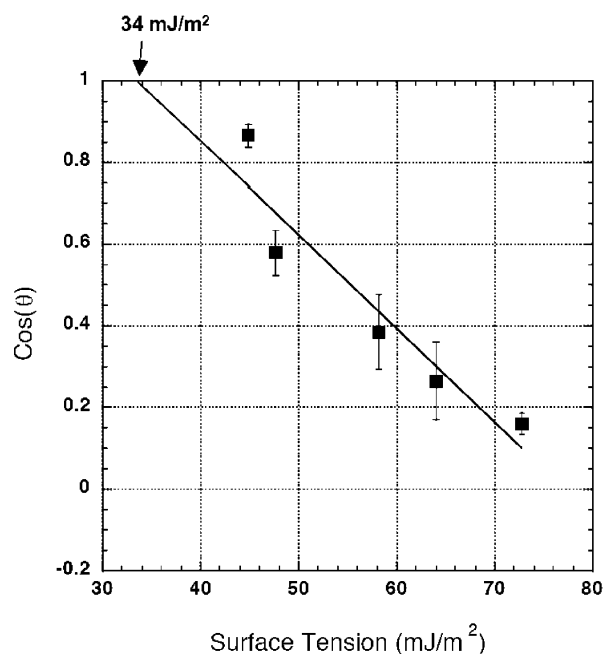


**Figure 9.** Plot of the average cosine of the contact angle measured for several liquids of varying surface tension on pentacene films. The error bars are one standard deviation of angles measured from several droplets of each liquid. A linear fit to the data, extrapolated to  $\cos(\theta) = 1$ , gives a critical surface tension of 34 mJ/m<sup>2</sup> for pentacene in air.

equilibrium. We believe this near-equilibrium growth shape is achieved by the combination of a high-temperature substrate (>100 °C) and the rather fast evaporation rate given by the flame heat source. The high substrate temperature gives sufficient molecular motion to determine the preferred state, as opposed to diffusion-limited aggregation, which is often seen when pentacene is grown on room-temperature substrates.<sup>14</sup> The fast evaporation rate ensures that the pentacene does not resublime into the vapor phase with additional heating.

Contact angle measurements were performed to determine the critical surface tension of pentacene thin films in air. We deposited droplets of various liquids, each with different surface tensions, onto the (001) textured pentacene thin films using a syringe under ambient laboratory conditions. The liquids used were diethylene glycol ( $\gamma = 44.8$  mJ/m<sup>2</sup>), ethylene glycol ( $\gamma = 47.7$  mJ/m<sup>2</sup>), formamide ( $\gamma = 58.2$  mJ/m<sup>2</sup>), glycerol ( $\gamma = 64.0$  mJ/m<sup>2</sup>), and water ( $\gamma = 72.8$  mJ/m<sup>2</sup>). The contact angle,  $\theta$ , was measured as the angle between the liquid–pentacene and air–liquid interfaces at the triple point. A plot of  $\cos(\theta)$  versus the liquid surface tension is shown in Figure 9. The data points are the average of the contact angles observed from several droplets of each liquid, with the error bars representing one standard deviation. A linear fit to the data, extrapolated to  $\cos(\theta) = 1$ , gives the critical surface tension of pentacene. This corresponds to the value of the liquid surface tension that would completely wet pentacene. The value of the critical surface tension for (001) textured pentacene thin films in air obtained from this extrapolation is 34 mJ/m<sup>2</sup>. We have simulated the (001) surface energy of pentacene to be 76 mJ/m<sup>2</sup> by expanding the *c*-axis lattice parameter and calculating the energy added to the system, and this value is considerably higher. The calculated value of 76 mJ/m<sup>2</sup> corresponds to the energy of the solid–vacuum interface. The surface energy of a material is often defined as the equilibrium energy of the solid–vapor interface, where the solid and the vapor are different phases of the same material. Our value of 76 mJ/m<sup>2</sup> for the pentacene solid–vacuum interfacial

energy is expected to be higher than the pentacene solid–vapor energy. The pentacene solid–vapor energy is in turn expected to be higher than the energy of the pentacene–air interface, which we have measured to be 34 mJ/m<sup>2</sup>. This value can be compared with the surface energies of thin films other than conductive organic materials, such as polyaniline, polypyrrole, and poly(3-hexylthiophene), whose surface energies were measured using methods similar to those described in this paper to be 45, 44, and 37 mJ/m<sup>2</sup>, respectively.<sup>27</sup>

The surface energy calculations from force field-based atomistic simulations presented here give values slightly different than those calculated for pentacene using first-principles calculations.<sup>18</sup> The trends are the same, however, with the (001) surface energy lower than any other, and the other low-index lattice planes having energies approximately 1.5–2 times larger than the (001) surface. Northrup et al.<sup>18</sup> predict an (001) energy of 50 mJ/m<sup>2</sup> using first-principles pseudopotential density-functional theory. The energies were calculated from an older crystal structure model<sup>28</sup> that has more recently been revised.<sup>5</sup> This older model<sup>28</sup> has been shown<sup>29</sup> to correspond to a distinct local energy minimum on the pentacene potential energy landscape that is slightly higher in energy than the global minimum structure given in ref 5. It is possible that the surface energies of this distinct structure<sup>28</sup> are lowered at the expense of an increase in bulk energy. Similar arguments were used to explain the existence of thickness-driven phase transformations in pentacene<sup>12</sup> and alumina.<sup>30</sup> Another explanation for the discrepancy between the surface energy values reported here and in ref 18 may simply be the parametrization of the Dreiding force field. The COMPASS, Dreiding, PCFF, CFF, and Universal force fields were tested on both pentacene and anthracene, and it was found that Dreiding best predicted the lattice parameters and planarity of the molecule. Calculations of the anthracene surface energies using the Dreiding force field and the methods described here also showed good agreement with an earlier work, which calculated the (001) surface energy of anthracene to be 75 mJ/m<sup>2</sup>.<sup>19</sup> From experimental measurements of crystal face areas, such as the data presented in this work, only relative values of surface energies can be obtained, and our force field-based calculations show good relative agreement with both the experimental data and the first-principles calculations.<sup>18</sup>

Many processes used to grow pentacene films have used lower (RT) substrate temperatures and are dominated by kinetics. The resulting thin films have fern-shaped or dendritic morphologies.<sup>3,14</sup> Slow vapor growth of pentacene crystals can yield thin, platelike crystals in which the (001) faces are significantly larger than the other faces, which themselves are rarely faceted.<sup>5,31</sup> It is not yet clear which film morphology, faceted or dendritic, will yield the best electrical conductivity. The dendritic films may have interfaces and holes within a crystal grain, where two dendrite arms have grown together. However, more faceted films may suffer from larger gaps between neighboring crystals.<sup>17</sup> It may be possible to fill in these holes between large crystals with a second deposition of a soluble molecule such as a precursor that can be converted to pentacene in the solid state.<sup>32</sup> A recently published electrostatic AFM study of pentacene transport suggested that the traps were not obviously associated with the grain boundaries, however.<sup>33</sup> This study may indicate that the transport is dominated by the structure near the active layer–dielectric layer interface, and this is not easy to correlate with what is seen using AFM.

The control of film texture is expected to be a key step in producing high-quality devices. As the degree of texturing is

increased and polycrystalline films approach the single crystal-line limit, the number of transport limiting defects will be reduced and the overall carrier mobility will increase. Using X-ray diffraction, we have seen that growth onto flat mica and amorphous carbon-coated mica substrates can produce textured films with the (001) planes parallel to the substrate to within 3°. It is expected that slower growth rates onto even smoother substrates will improve this (001) texturing. In-plane texture may also be achieved by growth onto rubbed<sup>34</sup> or stepped<sup>35</sup> substrates. This will reduce the number and severity of (*hk*0) type grain boundaries. In the technologically relevant thin film field effect transistor, electrons and holes are likely to move in only the first few layers of pentacene closest to the dielectric substrate. It will therefore be most important to control and optimize the morphology of this region.

## Conclusions

We have used molecular simulation methods to calculate the surface energies of pentacene. Thin films of pentacene were grown by vacuum sublimation, and their crystal structure, degree of texturing, and morphology were analyzed using various microscopy and diffraction techniques. The films had a faceted morphology with a grain size of 1–20  $\mu\text{m}$ , and they were textured with the (001) planes parallel to the substrate within a 3° tolerance. The crystal face areas were measured experimentally using SEM and compared to the face areas as calculated from simulations. It was found that the pentacene crystals approached an equilibrium growth shape similar to that obtained from surface energy calculations.

**Acknowledgment.** We thank the NSF-sponsored IGERT program for Molecularly Designed Electronic, Photonic and Nanocrystalline Materials at the University of Michigan, the Undergraduate Research Opportunities Program at the University of Michigan, and the National Science Foundation (Grants DMR-0084304, DMR-9707975, and DMR-0518079) for funding.

## References and Notes

- (1) Klauk, H.; et al. *J. Appl. Phys.* **2002**, 92 (9), 5259.
- (2) Gundlach, D. J.; Lin, Y.-Y.; Jackson, T. N.; Nelson, S. F.; Schlom, D. G. *IEEE Electron Device Lett.* **1997**, 18, 87.
- (3) Nelson, S. F.; Lin, Y.-Y.; Gundlach, D. J.; Jackson, T. N. *Appl. Phys. Lett.* **1998**, 72 (15), 1854.
- (4) Dimitrakopoulos, C. D. *Adv. Mater.* **1999**, 11 (16), 1372.
- (5) Holmes, D.; Kumaraswamy, S.; Matzger, A. J.; Vollhardt, K. P. *C. Chem.—Eur. J.* **1999**, 5, 3399.
- (6) Mattheus, C. C.; et al. *Acta Crystallogr.* **2001**, C57 (8), 939.
- (7) Jentzsch, T.; Juepner, H. J.; Brzezinka, K.-W.; Lau, A. *Thin Solid Films* **1998**, 315, 273.
- (8) Bouchoms, I. P. M.; Schoonveld, W. A.; Vrijmoeth, J.; Klapwijk, T. M. *Synth. Met.* **1999**, 104, 175.
- (9) Dimitrakopoulos, C. D.; Brown, A. R.; Pomp, A. *J. Appl. Phys.* **1999**, 80, 2501.
- (10) Laquindanum, J. G.; Katz, H. E.; Lovinger, A. J.; Dodabalapur, A. *Chem. Mater.* **1996**, 8, 2542.
- (11) Minitaka, T.; Imai, H.; Ozaki, M.; Saco, K. *J. Appl. Phys.* **1992**, 72, 5220.
- (12) Drummy, L. F.; Martin, D. C. *Adv. Mater.* **2005**, 17, 903.
- (13) Drummy, L. F.; Kübel, C.; Lee, D.; White, A.; Martin, D. C. *Adv. Mater.* **2002**, 14 (1), 54.
- (14) Meyer zu Heringdorf, F. J.; Reuter, M. C.; Tromp, R. M. *Nature* **2001**, 412, 517.
- (15) Ruiz, R.; et al. *Chem. Mater.* **2004**, 16, 4497.
- (16) Dimitrakopoulos, C. D.; Malefant, P. R. L. *Adv. Mater.* **2002**, 14 (2), 99.
- (17) Bao, Z. N.; Lovinger, A. J.; Dodabalapur, A. *Adv. Mater.* **1997**, 9, 42.
- (18) Northrup, J. E.; Taigo, M. L.; Louie, S. G. *Phys. Rev. B* **2002**, 66, 121404.
- (19) Kitaigorodsky, A. I.; Ahmed, N. A. *Acta Crystallogr.* **1972**, A28, 207.
- (20) Winn, D.; Doherty, M. F. *AIChE J.* **2000**, 46 (7), 1348.
- (21) Mayo, S. L.; Olafson, B. D.; Goddard, W. A. *J. Phys. Chem.* **1990**, 94, 8897.
- (22) Roberts, R. J.; Payne, R. S.; Rowe, R. C. *Eur. J. Pharm. Sci.* **2000**, 9, 277.
- (23) Martin, D. C.; Thomas, E. L. *Polymer* **1995**, 36, 1743.
- (24) Brillante, A.; et al. *Chem. Phys. Lett.* **2002**, 357, 32.
- (25) Hartman, P.; Perdok, W. *Acta Crystallogr.* **1955**, 8, 49.
- (26) Wulff, G. *Z. Kristallogr.* **1901**, 34, 449.
- (27) Liu, M. J.; Tzou, K.; Gregory, R. V. *Synth. Met.* **1994**, 63, 67.
- (28) Campbell, R. B.; Robertson, J. M.; Trotter, J. *Acta Crystallogr.* **1962**, 15, 289.
- (29) Venuti, E.; Della Valle, R. G.; Brillante, A.; Masino, M.; Girlando, A. *J. Am. Chem. Soc.* **2002**, 124, 2128.
- (30) McHale, J. M.; Auroux, A.; Perrotta, A. J.; Navrotsky, A. *Science* **1997**, 277, 788.
- (31) Laudise, R. A.; Kloc, C.; Simpkins, P. G.; Siegrist, T. *J. Cryst. Growth* **1998**, 187, 449.
- (32) Afazi, A.; Dimitrakopoulos, C. D.; Breen, T. L. *J. Am. Chem. Soc.* **2002**, 124 (30), 8813.
- (33) Muller, E.; Marohn, J. *Adv. Mater.* **2005**, 17, 1410.
- (34) Swiggers, M. L.; et al. *Appl. Phys. Lett.* **2001**, 79 (9), 1300.
- (35) Ossó, J. O.; et al. *Adv. Funct. Mater.* **2002**, 12 (6–7), 455.